nanomaterials

MDPI

Article

Engineering a Novel $AgMn_2O_4$@$Na_{0.55}Mn_2O_4$ Nanosheet toward High-Performance Electrochemical Capacitors

Guiling Wang [1], Zihao Liu [1], Chenchao Ma [1], Zhiling Du [1,2,*], Dongyan Liu [1], Kun Cheng [1], Xiangju Ye [1], Tingting Liu [3,4] and Lei Bai [1,*]

[1] College of Chemistry and Materials Engineering, Anhui Science and Technology University, Bengbu 233030, China; wangguilingcg@126.com (G.W.); lzh2304971627@163.com (Z.L.); mcc13212022@163.com (C.M.); eivleivl@163.com (D.L.); ck482845261@163.com (K.C.); yexiangju555@126.com (X.Y.)
[2] School of Energy and Environmental, Hebei University of Engineering, Handan 056038, China
[3] Provincial Key Laboratory of Polyolefin New Materials, College of Chemistry & Chemical Engineering, Northeast Petroleum University, Daqing 163318, China; 2008little@163.com
[4] Northeast Petroleum University at Qinhuangdao, Qinhuangdao 066004, China
* Correspondence: zhilingdu@hebeu.edu.cn (Z.D.); baileiwj2014@163.com (L.B.)

Abstract: Manganese oxides, as a type of two-dimensional (2D) material with high specific area and low cost, are considered promising energy storage materials. Here, we report novel $AgMn_2O_4$/$Na_{0.55}Mn_2O_4$ nanosheets created by a popular liquid precipitation method with different $AgNO_3$ contents, and their corresponding physical and electrochemical characterizations are performed. The results show that the ultra-thin $Na_{0.55}Mn_2O_4$ nanosheets were combined with the $AgMn_2O_4$ nanoparticles and an enhancement in their specific capacity was observed compared to the pristine sheets. This electrode material displays a peak specific capacitance of 335.94 F g^{-1} at 1 A g^{-1}. Using an asymmetric supercapacitor (ASC) assembled using a positive electrode made of $AgMn_2O_4$/$Na_{0.55}Mn_2O_4$ nanosheets and a reduced graphene oxide (rGO) negative electrode, a high energy density of 65.5 Wh kg^{-1} was achieved for a power density of 775 W kg^{-1}. The ASC showed good cycling stability with a capacitance value maintained at 90.2% after 10,000 charge/discharge cycles. The excellent electrochemical performance of the device was ascribed to the heterostructures and the open space formed by the interconnected manganese oxide nanosheets, which resulted in a rapid and reversible faraday reaction in the interface and further enhanced its electrochemical kinetics.

Keywords: supercapacitor; two-dimensional (2D) materials; $Na_{0.55}Mn_2O_4$; $AgMn_2O_4$

Citation: Wang, G.; Liu, Z.; Ma, C.; Du, Z.; Liu, D.; Cheng, K.; Ye, X.; Liu, T.; Bai, L. Engineering a Novel $AgMn_2O_4$@$Na_{0.55}Mn_2O_4$ Nanosheet toward High-Performance Electrochemical Capacitors. *Nanomaterials* **2022**, *12*, 1538. https://doi.org/10.3390/nano12091538

Academic Editor: Nikos Tagmatarchis

Received: 4 April 2022
Accepted: 28 April 2022
Published: 2 May 2022

1. Introduction

Supercapacitors are considered to be some of the most promising candidates among energy-storage devices due to their inherent advantages, such as high specific capacitance, high power density, superior rate capability, outstanding durability, and excellent environmental compatibility [1–3]. The electrode materials of supercapacitors play a crucial role in energy storage through electrical double layer capacitors (EDLC) and pseudocapacitors. In recent years, various electrode materials have been reported in the field of supercapacitors, such as carbon materials [4–6], transition metal oxides, [7–11], sulfide [12,13], polyaniline [8,14], and metal organic frameworks [15–17].

Two-dimensional (2D) manganese oxides, as hot energy storage materials for batteries, have attracted extensive attention due to their unique physical and chemical properties since they were discovered [18–21]. Currently, 2D materials are widely selected as electrode materials to enhance specific capacitance due to their high specific surface area for double-layer capacitance and more active sites for pseudocapacitance. However, their characteristics of reunion and volume expansion/contraction during the charge-discharge process greatly limit their advantages, resulting in descending cyclic stability.

Thus, many efforts have also been made to improve electrochemical performance by coupling the active phase with conductive carbon materials and doping heteroatom [22,23]. Recently, Wan et al. [24] found that δ-$Al_{0.06}MnO_2$ showed a larger specific capacitance of 450 mF cm^{-2} at a current density of 0.1 mA cm^{-2} than that of δ-MnO_2 (420 mF cm^{-2} at 0.1 mA cm^{-2}) and that its capacitance retention was enhanced from 75% for pure δ-MnO_2 to 84% in δ-$Al_{0.1}MnO_2$ after 5000 cycles. Hu et al. [25] prepared Cu^{2+} intercalated δ-MnO_2 and, through bader charge analysis, demonstrated that the Cu^{2+} intercalation decreased the average valence state of Mn, thus creating more redox-active sites in bulk MnO_2. Zarshad et al. [26] reported on the core-shell heterostructure of birnessite-type Fe-doped manganese oxides. The Fe-MnO_2 electrodes displayed a specific capacitance of about 350 F g^{-1} at a current density of 1 A g^{-1} and presented an excellent cycling performance with capacitance retention of 88.8% after 6000 cycles at a current density of 10 A g^{-1}. The above studies confirm that heteroatom doping is considered an effective method for improving the properties of manganese dioxide electrode materials.

In this paper, novel $AgMn_2O_4$@$Na_{0.55}Mn_2O_4$ nanosheets were prepared by liquid phase precipitation method. Silver ions were first precipitated into Ag_2O nanoparticles, subsequently converted into $AgMn_2O_4$ and then further intercalated onto the growing $Na_{0.55}Mn_2O_4$ nanosheets, which significantly enhances the electron transferability between the conductive $AgMn_2O_4$ particles and $Na_{0.55}Mn_2O_4$ nanosheets. In addition, the influence of morphology on the electrochemical properties of the doped products was studied. $AgMn_2O_4$@$Na_{0.55}Mn_2O_4$ displayed the best specific capacitance of 335.94 F g^{-1} at 1 A g^{-1}, which was higher than the $Na_{0.55}Mn_2O_4$ nanosheets' capacitance of 118.7 F g^{-1}.

2. Materials and Methods

2.1. Material Synthesis

All reagents were of analytical grade and were used as received without further purification. $AgMn_2O_4$@$Na_{0.55}Mn_2O_4$ nanosheets were synthesized using a facile chemical deposition method. Typically, 0.0028 mol manganese acetate and a certain silver nitrate content, 1.16 g EDTA and 50 mg SDS were dissolved in 50 mL of deionized water and stirred for about 1 h. Note that silver nitrate content was controlled by tuning the molar ratio for silver to manganese to 0%, 5%, 10%, and 15%, respectively. Then, 50 mL of 0.25 M NaOH aqueous solution was subsequently added to the above solution and 50 mL 0.12 M $K_2S_2O_8$ aqueous solution was dripped into the mixture solution and stirred continuously to obtain the precipitation product through a chemical deposition reaction. Finally, the solution was maintained at a constant temperature in a water bath of 30 °C for 12 h, resulting in the targeted production of silver-doped ultrathin manganese oxide nanosheets. The samples synthesized with different silver to manganese molar ratios of 0%, 5%, 10%, 15% were respectively notated as Mn-Ag-0.00, Mn-Ag-0.05, Mn-Ag-0.10, and Mn-Ag-0.15.

2.2. Structure Characterization

The powder X-ray diffraction (XRD) patterns were carried out on a RigakuSmart Lab X-ray diffractometer (Jena, Germany) with Cu Kα radiation (λ = 0.1541 nm, operated at 40 kV and 40 mA) at a scanning rate of 20° min^{-1} to determine the structures of samples. Transmission electron microscopy (TEM) was performed on a Hitachi HT7700 (Tokyo, Japan) at an acceleration voltage of 120 kV and scanning electron microscope (SEM) images were gained using a Carl Zeiss Super55 (Jena, Germany) operating at an accelerating voltage of 5 kV to examine the morphologies and microstructures. X-ray photoelectron spectroscopy (XPS) studies were conducted on a Thermo (Shanghai, China) using Al K (=1486.6 eV) radiation, operated at an accelerating voltage of 12.5 kV.

2.3. Electrochemical Properties

All related electrochemical characterizations were measured by a CHI 660E electrochemical workstation (CH Instrument, Chenhua Co., Shanghai, China) in 6 M KOH via a typical three-electrode system. The preparation of MnO_2-based electrodes and electrochemical characterizations were similar to our previously reported work [27], and the loading amount of the active material was about 3.0 mg cm^{-2} in electrochemical experiments. A two-electrode system was designed to analyze the power and energy density of a manganese oxide asymmetric supercapacitor (Mn-Ag-0.10//rGO). A battery test instrument system (BST4008, Xinwei, China) was used to characterize the cycling performance of the ASC device. The ASC devices were prepared using nanomaterials (Mn-Ag-0.10) as the positive electrode with the rGO as the negative electrode (Figures S1–S3) in 6 M KOH electrolyte. The mass ratio between the positive and negative electrode materials was 1:2. The stable potential window was −1.0~−0.2 V for the rGO electrode and 0~0.55 V for the Ag-0.10 electrode. The energy density was calculated by using the following equation:

$$E = 1/2C_{cell}V^2$$

where C_{cell} is the total cell specific capacitance and V is the cell-operation potential. The average power density was calculated by using the following equation:

$$P = E/\Delta t$$

where E is the energy density and Δt is the discharge time.

3. Results and Discussion

The formation mechanism of $AgMn_2O_4$@$Na_{0.55}Mn_2O_4$ nanolamellar structure is shown in Figure 1. When EDTA-Na_2 was added to an $Mn(Ac)_2$-$AgNO_3$ mixed solution, it was easier to generate a stable EDTA-Mn complex due to the relatively large coordination constant K_f (lgK_f = 13.87) between Mn^{2+} and EDTA. However, the coordination constant K_f of EDTA-Ag formed by Ag^+ and EDTA was relatively small (lgK_f = 7.32). When the precipitant NaOH was added, free Ag^+ would first precipitate with NaOH to generate AgOH and further dehydrate to form black Ag_2O nanoparticles. Conversely, the precipitation process generated by Mn^{2+} and NaOH was slow for a large coordination equilibrium constant K_f. $AgMn_2O_4$ was formed and intercalated onto the growing $Na_{0.55}Mn_2O_4$ nanosheet by the reciprocal actions between Ag_2O nanoparticles and EDTA-Mn. Owing to the in-situ growing process, the $AgMn_2O_4$ and $Na_{0.55}Mn_2O_4$ interacted with each other by intermolecular forces. The formation of a heterojunction structure could lead to excellent structural stability, which would allow the electrode to maintain good electrochemical performance during the charge-discharge process.

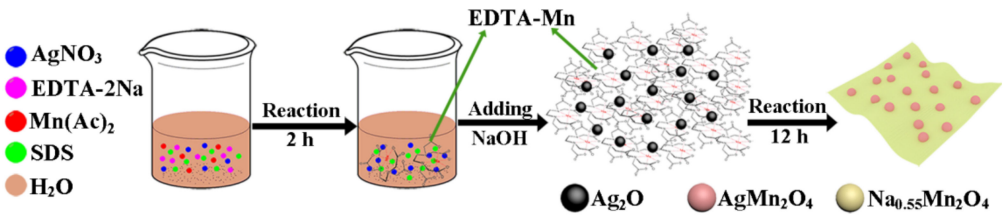

Figure 1. Schematic illustration of the formation mechanism of $AgMn_2O_4$@$Na_{0.55}Mn_2O_4$ nanosheets.

3.1. XRD Analysis

It is noted from Figure 2 that the XRD patterns of Mn-Ag-0.00, Mn-Ag-0.05, Mn-Ag-0.10, and Mn-Ag-0.15 show obvious diffraction peaks, attributed to the $Na_{0.55}Mn_2O_4$ (PDF#43-1456). The XRD patterns of Mn-Ag-0.05 and Mn-Ag-0.10 present the minor peaks of the impurities indicated by the asterisk, which were indexed to $AgMn_2O_4$(PDF#16-0740). However, the diffraction peaks for $Na_{0.55}Mn_2O_4$ and $AgMn_2O_4$ weakened and no $AgMn_2O_4$-related peaks were detected as the molar ratio of silver to manganese increased to 15% (Mn-Ag-0.15). From this phenomenon, it is speculated that silver had a great effect on the crystallinity of $Na_{0.55}Mn_2O_4$ by affecting the ion as a liquid, and the $Na_{0.55}Mn_2O_4$ directly related to the formation of $AgMn_2O_4$.

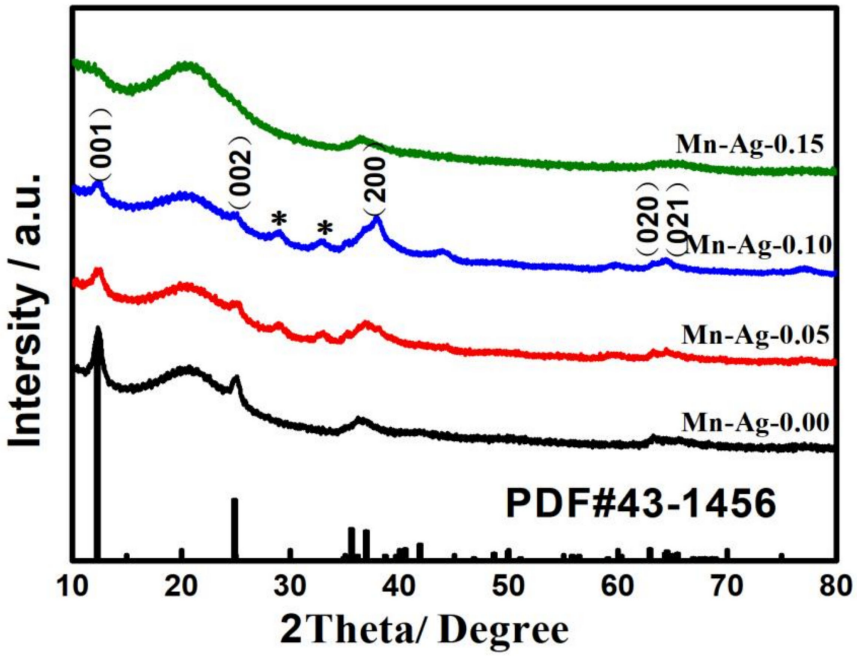

Figure 2. XRD patterns of Mn-Ag-0.00, Mn-Ag-0.05, Mn-Ag-0.10, and Mn-Ag-0.15 samples.

XPS measurements were performed to investigate the surface metal oxidation states of Mn-Ag-0.10. Figure 3A shows the M 2p transitions. The binding energies of Mn $2p_{3/2}$ and Mn $2p_{1/2}$ are 642.33 and 653.9 eV, which can be attributed to a mixture of Mn^{4+} and Mn^{3+} [28]. Figure 3B displays the XPS of Ag 3d. The Ag $3d_{5/2}$ and Ag $3d_{3/2}$ peaks are 368.1 and 374.1 eV, which are characteristic of Ag^{+} [29].

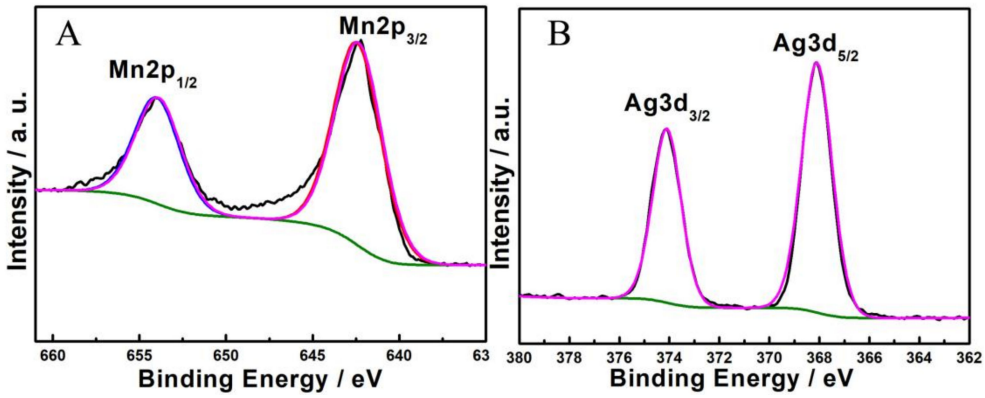

Figure 3. XPS of Mn-Ag-0.10: (**A**) Mn 2p (**B**) Ag 3d.

3.2. Effect of Doping on Morphology

The SEM images of Ag-0.00, Ag-0.05, Ag-0.10, and Ag-0.15 are shown in Figure 4. It was suggested that the morphological qualities of the materials changed obviously after adding silver ions. The material presented an irregular layered structure (Figure 4A) when no silver was added. The lamellars recombined into spherical nanoflowers after the silver with the the molar ratio to manganese of 5% and 10% were added, as shown in Figure 4B,C. The lamellar and spherical nanoflower structures provided high specific surface area and many pores, which could be conduced to expose more active area for charge storage, shorten the charge transfer pathway, and accelerate the electrochemical reaction, respectively. However, with an increase of the silver ion concentration to 15% (Figure 4D), the solid was agglomerated into particles. EDS (Figures 4E and S4) of Ag-0.10 was used to analyze the distribution of silver in the sample and it was found that the silver was uniformly distributed and no large area partial set was noticed.

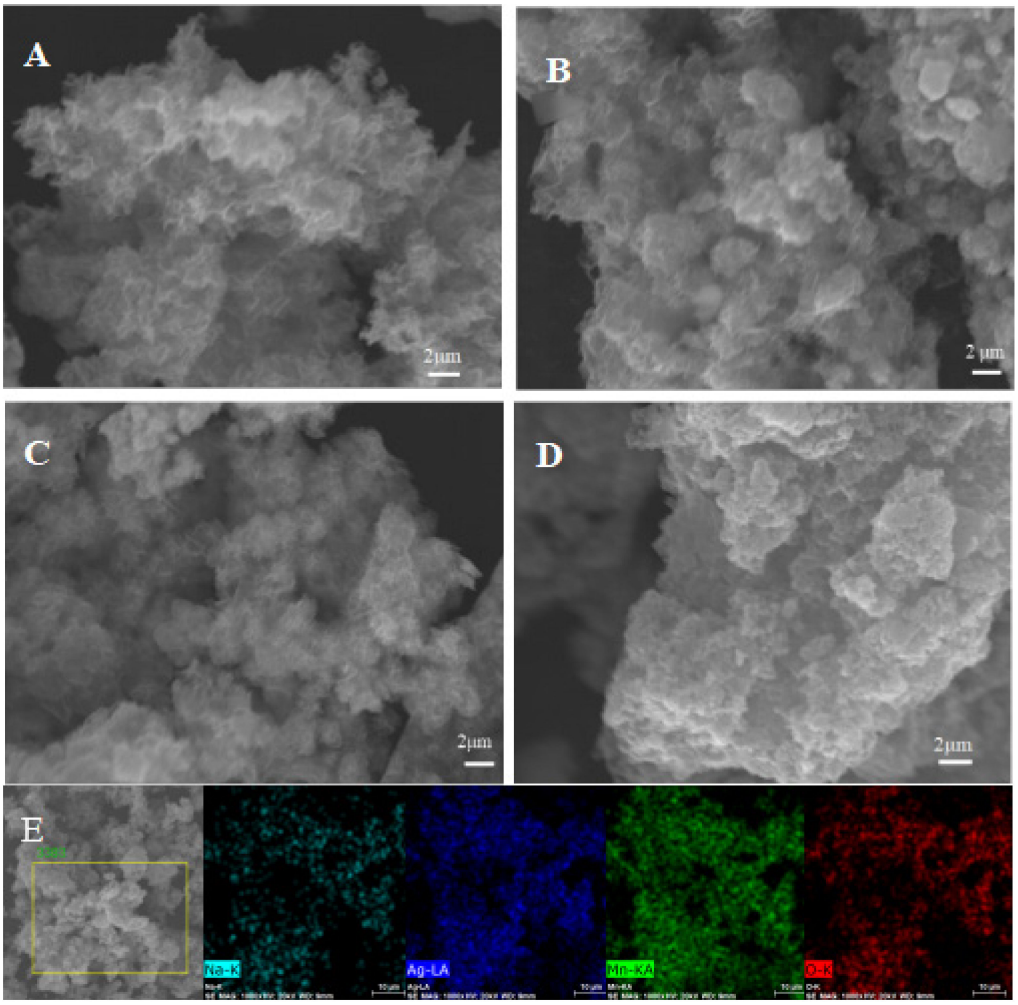

Figure 4. SEM images of (**A**) Mn-Ag-0.00, (**B**) Mn-Ag-0.05, (**C**) Mn-Ag-0.10, (**D**) Mn-Ag-0.15, and mapping of (**E**) Mn-Ag-0.10.

In addition, transmission electron microscopy (TEM) was performed on Mn-Ag-0.00 and Mn-Ag-0.10 and their morphological and internal structure properties were analyzed. In Figure 5A–C, Mn-Ag-00 shows an ultra-thin nanosheet structure. This nanosheet was a multi-layer structure formed by about ten layers of manganese oxide. After Ag^+ was added (Figure 5D–F), the finer flaky spherical aggregates formed and many small particles adhered to the surface of the nanosheet. A HRTEM image (Figure 5F) displays that the small particles had lattice fringes of 0.3 nm and could be identified as $AgMn_2O_4$, while

the manganese oxide had no obvious lattice structure. Figure 5G shows the EDS mapping of Figure 5D. It can be seen that $AgMn_2O_4$ was uniformly dispersed on the $Na_{0.55}Mn_2O_4$ nanosheets, which is consistent with the results of SEM. The homogeneous distribution of Ag and Mn elements illustrated the in situ formation of $AgMn_2O_4$ in the $Na_{0.55}Mn_2O_4$ matrix, a state which will typically result in the formation of heterostructures and intimate contact between the components [30,31].

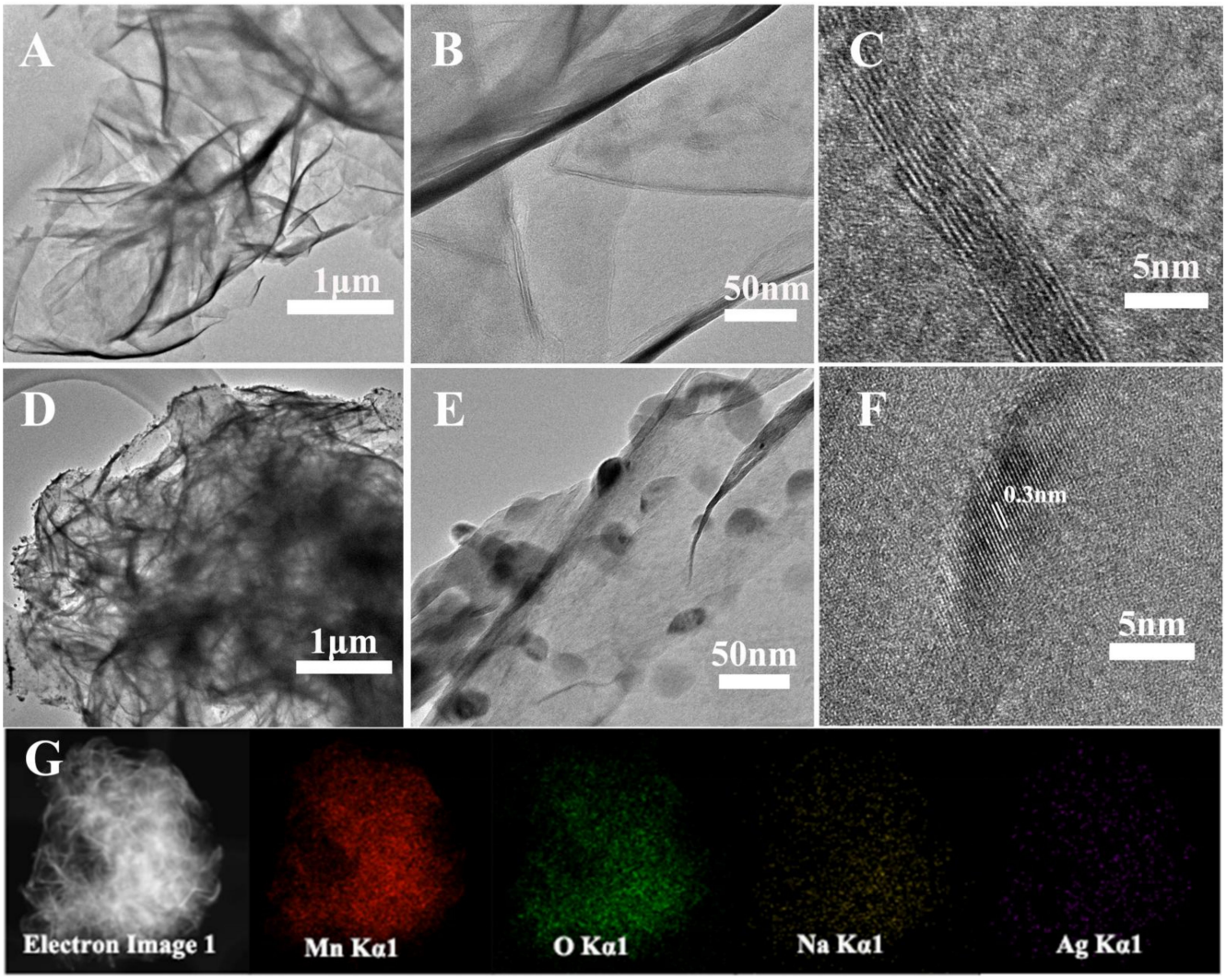

Figure 5. TEM images of Mn-Ag-0.00 (**A**–**C**), Mn- Ag-0.10 (**D**–**F**), and mapping of Mn-Ag-0.10 (**G**).

To investigate the capacitive property of the new phase of $AgMn_2O_4$@$Na_{0.55}Mn_2O_4$, we first evaluated the CV curves of the different samples, as shown in Figure 6A. The curves suggest a pair of distinct redox peaks at ca. 0.4 V and 0.1 V, which resulted from the insertion/extraction of ions during the charge and discharge process [32], the increased trend of current intensity with the added silver content, and the decreased trend as the molar ratio rose up to 15%. It is obvious that the maximum current response was achieved when the silver content was 10%. This result indicates that the sample of Mn-Ag-0.10 possessed the best pseudocapacitance properties, ascribed to the formation of a new phase of $AgMn_2O_4$. The values of these samples were 167.84 F g^{-1}, 233.54 F g^{-1}, 248.23 F g^{-1}, and 191.92 F g^{-1}.

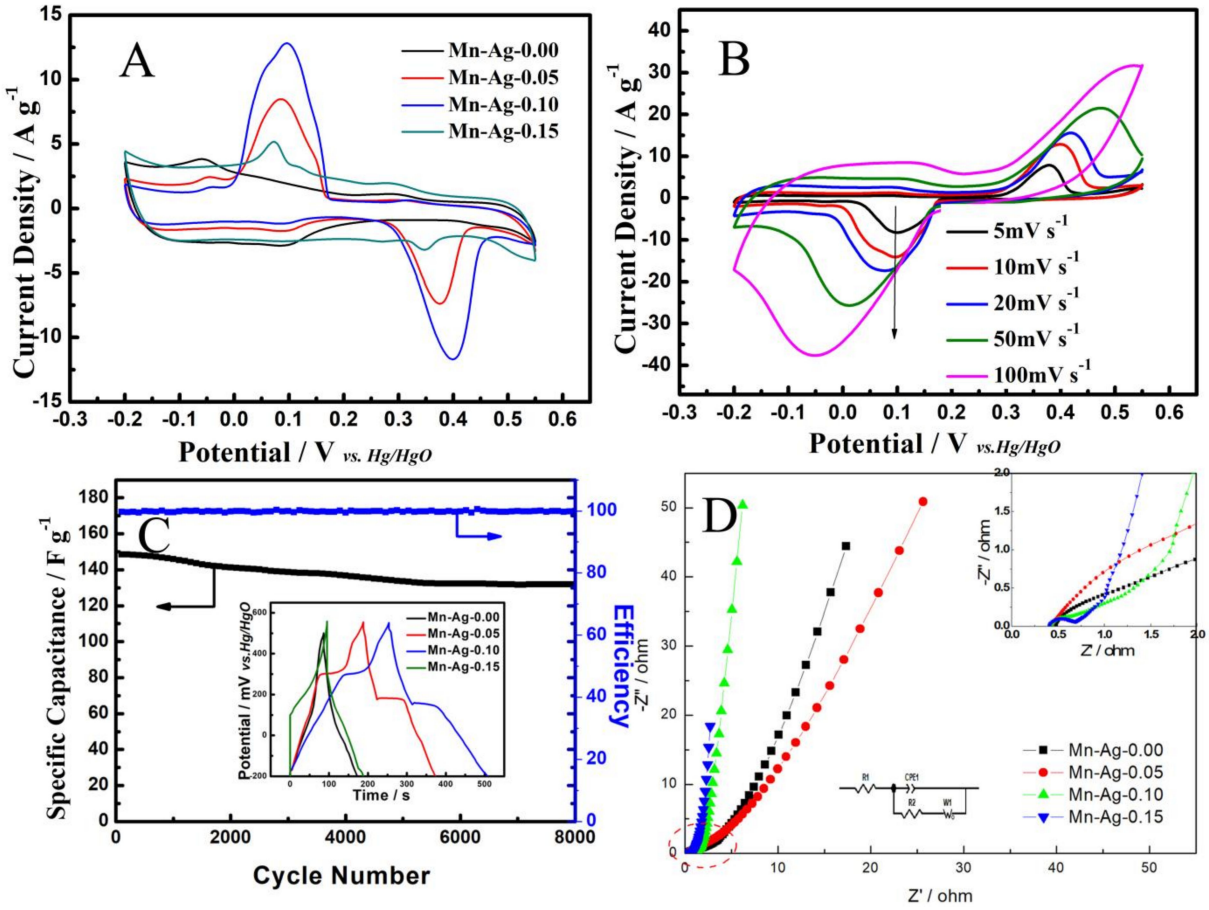

Figure 6. Electrochemical performance of synthesized samples. (**A**) CV curves at the scan rate of 10 mV s^{-1}. (**B**) CV curves of Ag-Mn-0.10 at different scan rates. (**C**) Lifetime and coulombic efficiency curves of Ag-Mn-0.10 at a high current density of 10 A g^{-1}. The insert in the bottom-left corner is the galvanostatic charge-discharge curves tested at 1 A g^{-1}. (**D**) Nyquist plots. The insert in the top-right corner is the enlarged Nyquist plot in the high frequency region.

Figure 6B shows the CV curves of the Mn-Ag-0.10 sample at various scanning rates (Mn-Ag-0.00, Mn-Ag-0.05, and Mn-Ag-0.15 are shown in Figure S5). The consecutive order change of the shapes of the CV curves with a scanning rate from 5 to 100 mV s^{-1} indicates reasonable capacitive behaviors and high-rate cyclability and stability. It can be calculated that the specific capacitances of Mn-Ag-0.10 at scanning rates of 5, 10, 20, 50, and 100 mV s^{-1} are 315.17, 248.23, 151.82, 139.51, and 101.19 F g^{-1}, respectively.

The galvanostatic charge-discharge curves are described in the insert of Figure 6C, where the electrodes were tested at 1 A g^{-1}. The values of Mn-Ag-0.00, Mn-Ag-0.05, Mn-Ag-0.10 and Mn-Ag-0.15 were 117.36 F g^{-1}, 250.15 F g^{-1}, 335.94 F g^{-1}, and 132.02 F g^{-1}. This change trend is consistent with the CV images. It can be seen that the Mn-Ag-0.10 (GCD curves of different samples tested at 2 A g^{-1}, 5 A g^{-1}, and 10 A g^{-1} are shown in Figure S6 and Table S1) exhibited the highest specific capacitance, which is consistent with the CV curves. Cycle stability is an important parameter in industrial fields and is explored in detail in Figure 6C. The Mn-Ag-0.10 sample at a high current density of 20 A g^{-1} presented excellent cycle durability with a high capacity retention of 88.80% from 148.46 F g^{-1} to 131.83 F g^{-1} after 8000 cycles. Additionally, the coulombic efficiency of Mn-Ag-0.10 was near 100%, which was due to the rapid and reversible faraday reaction in the interface between the active material and electrolyte.

To further explore the capacitive behaviors of the prepared samples, EIS analysis was performed over a frequency range from 100 kHz to 10 mHz. As clearly displayed in Figure 6D, the Nyquist plots in the low-frequency region are steeply and more perpen-

dicular to the real axis with the addition of the Ag-doped content. The plots of Ag-0.10 and Ag-0.15 display almost vertical slopes, indicating efficient diffusion of electrolyte ions to active material surfaces. Moreover, the Nyquist plots of all samples demonstrate shot x-intercepts and small diameters of the semicircle in high- and mild-frequency regions (Table S2). Mn-Ag-0.15 presents the smallest diameter, owing to the formation of the new phase, $AgMn_2O_4$. In view of all the above, the introduction of $AgMn_2O_4$ can lead to small charge-transfer resistances and superior capacitive performance. However, micromorphology plays a critical role in charge storage for supercapacitors, as suggested by the fact that the Mn-Ag-0.10 electrode exhibited the best electrochemical properties of all electrodes considering the combination effect of electrical conductivity and micromorphology.

The construction of an ASC device is generally considered an effective strategy to evaluate the application value of as-prepared electrodes in a real system [33–36].

The ASC of Mn-Ag-0.10//rGO at different scanning rates (5–100 mV s^{-1}) are shown in Figure 7A. A symmetrical CV shape was still maintained well even at scanning rates up to 100 mV s^{-1}, suggesting that the ASC device had a desirable charge-discharge property and perfect supercapacitor behavior. The rate performances for ASC device are shown in Figure 7B. The Mn-Ag-0.10//rGO was 78.3 F g^{-1} at 1 A g^{-1}, and when the current density rose up to 10 A g^{-1}, the capacitance value still remained at 49.9 F g^{-1}. The Ragone plot of the power density and the energy density of an asymmetric supercapacitor are crucial for evaluating the effect of a capacitor (Figure 7C). The Mn-Ag-0.10//rGO supercapacitor achieved an energy density of 65.5 kWh kg^{-1} at a power density of 775 W kg^{-1}. This supercapacitor maintained an energy density of 41.98 kW h kg-1 with a power density up to 7750 W kg^{-1}. The cycling stability and efficiency of this supercapacitor was measured by GCD test (Figure 7D, the inset of Figure 7D are GCD curves at different densities after 10,000 cycles). After 10,000 charge−discharge cycles at 1 A g^{-1}, the Mn-Ag-0.10//rGO electrode still maintained 90.2% capacitance retention. The electrochemical properties of the nanosheets of manganese oxides and their composite materials reported in the literature are listed in Table 1. It can be seen from the literature comparision that the Mn-Ag-0.10//rGO ASC prepared in this work is comparable. Its excellent electrochemical performance could be ascribed to the following advantages. On the one hand, the open space formed by the interconnected manganese oxide nanosheets greatly facilitates the transport of electrolyte, thus enhancing electrochemical kinetics. On the other hand, the heterostructures have excellent structural stability, which ensures the electrode maintains good electrochemical performance during the charge-discharge process.

Table 1. Comparison of the electrochemical performance of $AgMn_2O_4/Na_{0.55}Mn_2O_4$ nanosheets with other previously reported two-dimensional manganese oxides.

Materials	Specific Capacitance	Cycle Stability	Power Density	Energy Density	Reference
C@MnO nanosheets	162.7 F g^{-1}(0.5 A g^{-1})	93.5% (10 A g^{-1}) 5000 cycles (ASC)	400 W kg^{-1}	57.7 Wh kg^{-1}	[19]
$MnCo_2O_4$ nanoflakes	256 F g^{-1}(5 mV s^{-1})	85% (2 A g^{-1}) 10,000 cycles (ASC)	1000 W kg^{-1}	25 Wh kg^{-1}	[37]
lamellarMnO_2@Carbon nanocoil	435 F g^{-1}(1 A g^{-1})	92.7% (2 A g^{-1}) 5000 cycles (ASC)	100 W kg^{-1}	21.58 Wh kg^{-1}	[38]
$CoMn_2O_4$nanosheets /carbon nanotubes	732 F g^{-1}(2 mV s^{-1})	77% (100 mV s^{-1}) 5000 cycles (ASC)	400 W kg^{-1}	47.39 Wh kg^{-1}	[39]
Fe doped MnO_2 nanosheets	157 F g^{-1}(0.5 A g^{-1})	71.4% (0.5 A g^{-1}) 5000 cycles	1000 W kg^{-1}	30.3 Wh kg^{-1}	[40]
$AgMn_2O_4$/ $Na_{0.55}Mn_2O_4$ nanosheets	335.94 F g^{-1}(1 A g^{-1})	90.4% (10 A g^{-1}) 10,000 cycles (ASC)	775 W kg^{-1}	65.5 Wh kg^{-1}	This work

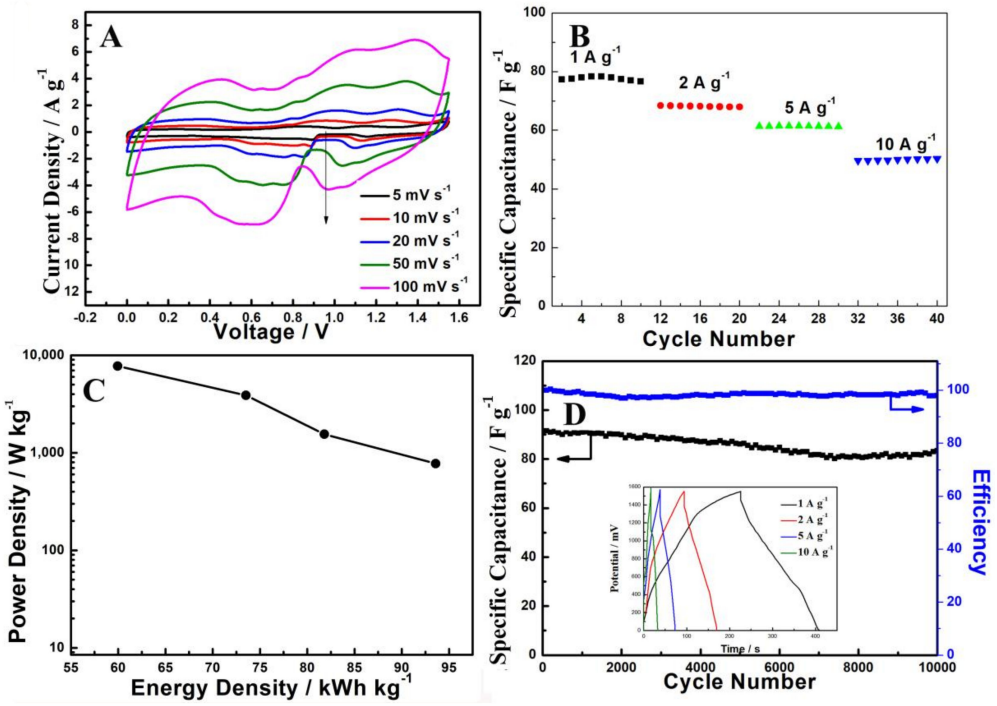

Figure 7. (**A**) CV curves of Mn-Ag-0.10//rGO at various scan rates (5–100 mV s^{-1}); (**B**) Rate performance of Ag-0.10//rGO; (**C**) Ragone plot of the energy density and the power density of Mn-Ag-0.10//rGO; (**D**) Cycling stability and coulombic efficiency of Mn-Ag-0.10//rGO. The insert is the galvanostatic charge-discharge curves tested at 1 A g^{-1}.

4. Conclusions

In summary, novel $AgMn_2O_4/Na_{0.55}Mn_2O_4$ nanosheets were synthesized with a popular liquid precipitation method for use as high-performance electrodes for supercapacitors. TEM images show that $AgMn_2O_4$ formed in situ in the $Na_{0.55}Mn_2O_4$ matrix, which resulted in the formation of heterostructures and the intimate contact between the components. The combination of $AgMn_2O_4$ nanoparticles and ultra-thin $Na_{0.55}Mn_2O_4$ nanosheets provided the electrodes with heterostructures with fast ion transport and a synergistic effect from the $AgMn_2O_4/Na_{0.55}Mn_2O_4$ hybrid electrodes. This electrode material displayed a peak specific capacitance of 335.94 F g^{-1} at 1 A g^{-1} in a three-electrode system. In addition, its discharge capacity at 10 A g^{-1} was slightly decreased, after 8000 cycles, fading from 148.46 to 131.83 F g^{-1}, and the corresponding capacitance retention was 88.8%. The Mn-Ag-0.10//rGO ASC had a high energy density of 65.5 Wh kg^{-1} at a power density of 775 W kg^{-1} and showed good cycling stability, with 90.2% capacitance value maintained after 10,000 charge/discharge cycles.

Supplementary Materials: The following supporting information can be downloaded at: https://www.mdpi.com/article/10.3390/nano12091538/s1, Figure S1: CV curves of rGO; Figure S2: The galvanostatic charge-discharge curve of rGO tested at 1 A g^{-1}; Figure S3: Cycle life curve of rGO at a current density of 2 A g^{-1}; Figure S4. EDS of Mn-Ag-0.10; Figure S5: CV curves of Mn-Ag-0.00,Mn-Ag-0.05, Mn-Ag-0.15 at different scan rates; Figure S6: GCD curves of Mn-Ag-0.00,Mn-Ag-0.05, Mn-Ag-0.10 and Mn-Ag-0.15 at (A) 2 A g^{-1}, (B) 5 A g^{-1} and (C) 10 A g^{-1}; Table S1: Specific Capacitance of Mn-Ag-0.00, Mn-Ag-0.05, Mn-Ag-0.10 and Mn-Ag-0.15 at different current density; Table S2: Rs and Rct values of Mn-Ag-0.00, Mn-Ag-0.05, Mn-Ag-0.10 and Mn-Ag-0.15 samples.

Author Contributions: Conceptualization, G.W. and Z.D.; methodology, G.W. and Z.L.; validation, G.W. and L.B.; formal analysis, C.M.; investigation, C.M., D.L.; resources, Z.L. and D.L.; data curation, Z.L., C.M., K.C. and X.Y.; writing—original draft preparation, G.W., Z.D. and T.L.; writing—review and editing, G.W.; supervision, Z.D. and L.B.; funding acquisition, G.W. All authors have read and agreed to the published version of the manuscript.

Funding: This research was funded by the Natural Science Projects of Anhui Province (1908085QB84, 1908085QB71) the Innovation Fund project of Hebei University of Engineering (SJ2101003075), Anhui Province Top Talent Project (gxbjZD28), the National Natural Science Foundation of China (51904077) and the Anhui College Student Innovation Plan (S202110879093).

Institutional Review Board Statement: Not applicable.

Informed Consent Statement: Not applicable.

Data Availability Statement: The data presented in this study are available on request from the corresponding author.

Conflicts of Interest: The authors declare no conflict of interest.

References

1. Qin, W.; Zhou, N.; Wu, C.; Xie, M.; Sun, H.; Guo, Y.; Pan, L. Mini-Review on the Redox Additives in Aqueous Electrolyte for High Performance Supercapacitors. *ACS Omega* **2020**, *5*, 3801–3808. [CrossRef] [PubMed]
2. Kumar, K.S.; Choudhary, N.; Jung, Y.; Thomas, J. Recent Advances in Two-Dimensional Nanomaterials for Supercapacitor Electrode Applications. *ACS Energy Lett.* **2018**, *3*, 482–495. [CrossRef]
3. Min, L.; Ahmed, A.; Pascal, R.; Sabine, S.; Rabah, B. High Performance Flexible Hybrid Supercapacitor Based on Nickel Hydroxide Deposited on Copper Oxide Supported by Copper Foam for a Sunlight-Powered Rechargeable Energy Storage System. *J. Colloid Interface Sci.* **2020**, *579*, 520–530.
4. Kumar, S.; Saeed, G.; Zhu, L.; Hui, K.N.; Kim, N.H.; Lee, J.H. 0D to 3D Carbon-Based Networks Combined with Pseudocapacitive Electrode Material for High Energy Density Supercapacitor: A Review. *Chem. Eng. J.* **2021**, *403*, 126352. [CrossRef]
5. Qi, B.; Ren, K.; Lin, Y.; Zhang, S.; Wei, T.; Fan, Z. Design of Layered-Stacking Graphene Assemblies as Advanced Electrodes for Supercapacitors. *Particuology* **2022**, *60*, 1–13. [CrossRef]
6. Shang, Z.; An, X.; Zhang, H.; Shen, M.; Baker, F.; Liu, Y.; Liu, L.; Yang, J.; Cao, H.; Xu, Q.; et al. Houttuynia-Derived Nitrogen-Doped Hierarchically Porous Carbon for High-Performance Supercapacitor. *Carbon* **2021**, *161*, 62–70. [CrossRef]
7. Low, W.H.; Khiew, P.S.; Lim, S.S.; Siong, C.W.; Ezeigwe, E.R. Recent Development of Mixed Transition Metal Oxide and Graphene/Mixed Transition Metal Oxide Based Hybrid Nanostructures for Advanced Supercapacitors. *J. Alloys Compd.* **2019**, *775*, 1324–1356. [CrossRef]
8. Abdah, M.A.A.M.; Azman, N.H.N.; Kulandaivalu, S.; Sulaiman, Y. Review of the Use of Transition-Metal-Oxide and Conducting Polymer-Based Fibres for High-Performance Supercapacitors. *Mater. Des.* **2020**, *186*, 108199. [CrossRef]
9. Venkatkarthick, R.; Qin, J. A New 3D Composite of V2O5-Based Biodegradable Ceramic Material Prepared by an Environmentally Friendly Thermal Method for Supercapacitor Applications. *Environ. Technol. Innov.* **2021**, *22*, 101474. [CrossRef]
10. Zhao, X.; Mao, L.; Cheng, Q.; Li, J.; Liao, F.; Yang, G.; Xie, L.; Zhao, C.; Chen, L. Two-Dimensional Spinel Structured Co-Based Materials for High Performance Supercapacitors: A Critical Review. *Chem. Eng. J.* **2020**, *387*, 124081. [CrossRef]
11. Sakib, M.N.; Ahmed, S.; Rahat, S.M.S.M.; Shuchi, S.B. A Review of Recent Advances in Manganese-Based Supercapacitors. *J. Energy Storage* **2021**, *44*, 103322. [CrossRef]
12. Yang, X.; Mao, J.; Niu, H.; Wang, Q.; Zhu, K.; Ye, K.; Wang, G.; Cao, D.; Yan, J. NiS_2/MoS_2 Mixed Phases with Abundant Active Edge Sites Induced by Sulfidation and Graphene Introduction Towards High-Rate Supercapacitors. *Chem. Eng. J.* **2021**, *406*, 126713. [CrossRef]
13. Iqbal, M.Z.; Khan, J. Optimization of Cobalt-Manganese Binary Sulfide for High Performance Supercapattery Devices. *Electrochim. Acta* **2020**, *368*, 137529. [CrossRef]
14. Xiong, C.; Li, M.; Zhao, W.; Duan, C.; Dai, L.; Shen, M.; Xu, Y.; Ni, Y. A Smart Paper@Polyaniline Nanofibers Incorporated Vitrimer Bifunctional Device with Reshaping, Shape-Memory and Self-Healing Properties Applied in High-Performance Supercapacitors and Sensor. *Chem. Eng. J.* **2020**, *396*, 125318. [CrossRef]
15. Bailmare, D.B.; Dhoble, S.J.; Deshmukh, A.D. Metal Organic Frameworks and Their Derived Materials for Capacity Enhancement of Supercapacitors: Progress and Perspective. *Synth. Met.* **2021**, *282*, 116945. [CrossRef]
16. Wang, D.-G.; Liang, Z.; Gao, S.; Qu, C.; Zou, R. Metal-Organic Framework-Based Materials for Hybrid Supercapacitor Application. *Coord. Chem. Rev.* **2020**, *404*, 213093. [CrossRef]
17. Chhetri, K.; Dahal, B.; Tiwari, A.P.; Mukhiya, T.; Muthurasu, A.; Ojha, G.P.; Lee, M.; Kim, T.; Chae, S.-H.; Kim, H.Y. Controlled Selenium Infiltration of Cobalt Phosphide Nanostructure Arrays from a Two-Dimensional Cobalt Metal–Organic Framework: A Self-Supported Electrode for Flexible Quasi-Solid-State Asymmetric Supercapacitors. *ACS Appl. Energy Mater.* **2021**, *4*, 404–415. [CrossRef]
18. Hu, Z.; Xiao, X.; Jin, H.; Li, T.; Chen, M.; Liang, Z.; Guo, Z.; Li, J.; Wan, J.; Huang, L.; et al. Rapid Mass Production of Two-Dimensional Metal Oxides and Hydroxides via the Molten Salts Method. *Nat. Commun.* **2017**, *8*, 15630. [CrossRef]
19. Zhao, N.; Deng, L.; Luo, D.; Zhang, P. One-Step Fabrication of Biomass-Derived Hierarchically Porous Carbon/MnO Nanosheets Composites for Symmetric Hybrid Supercapacitor. *Appl. Surf. Sci.* **2020**, *526*, 146696. [CrossRef]

20. Raj, C.J.; Manikandan, R.; Sivakumar, P.; Opar, D.O.; Savariraj, A.D.; Cho, W.J.; Jung, H.; Kim, B.C. Origin of Capacitance Decay for a Flower-like δ-MnO_2 Aqueous Supercapacitor Electrode: The Quantitative Surface and Electrochemical Analysis. *J. Alloys Compd.* **2021**, *892*, 162199.
21. Minakshi, M.; Nallathamby, K.; Mitchell, D.R. Electrochemical Characterization of an Aqueous Lithium Rechargeable Battery: The Effect of CeO_2 Additions to the MnO_2 Cathode. *J. Alloys Compd.* **2009**, *479*, 87–90. [CrossRef]
22. Chhetri, K.; Dahal, B.; Mukhiya, T.; Tiwari, A.P.; Muthurasu, A.; Kim, T.; Kim, H.; Kim, H.Y. Integrated Hybrid of Graphitic Carbon-Encapsulated Cu_xO on Multilayered Mesoporous Carbon from Copper MOFs and Polyaniline for Asymmetric Supercapacitor and Oxygen Reduction Reactions. *Carbon* **2021**, *179*, 89–99. [CrossRef]
23. Chhetri, K.; Tiwari, A.P.; Dahal, B.; Ojha, G.P.; Kim, H.Y. A ZIF-8-Derived Nanoporous Carbon Nanocomposite Wrapped with Co_3O_4-Polyaniline as an Efficient Electrode Material for an Asymmetric Supercapacitor. *J. Electroanal. Chem.* **2020**, *856*, 113670. [CrossRef]
24. Wan, J.; Ji, P.; Li, B.; Xi, Y.; Gu, X.; Huang, L.; He, M.; Hu, C. Enhanced Electrochemical Performance in an Aluminium Doped δ-MnO_2 Supercapacitor Cathode: Experimental and Theoretical Investigations. *Chem. Commun.* **2022**, *58*, 589–592. [CrossRef] [PubMed]
25. Hu, L.; Gao, R.; Zhang, A.; Yang, R.; Zang, X.; Wang, S.; Yao, S.; Yang, Z.; Hao, H.; Yan, Y.-M. Cu^{2+} Intercalation Activates Bulk Redox Reactions of MnO_2 for Enhancing Capacitive Performance. *Nano Energy* **2020**, *74*, 104891. [CrossRef]
26. Zarshad, N.; Wu, J.; Rahman, A.U.; Ni, H. Fe-MnO_2 Core-Shell Heterostructure for High-Performance Aqueous Asymmetrical Supercapacitor. *J. Electroanal. Chem.* **2020**, *871*, 114266. [CrossRef]
27. Chen, J.; Liu, Y.; Wang, G.; Guo, J.; Wang, X. Nickel-Doped Ultrathin K-Birnessite Manganese Oxide Nanosheet as Pseudocapacitor Electrode with Excellent Cycling Stability for High-Power Pesudocapacitors. *ACS Sustain. Chem. Eng.* **2017**, *5*, 1594–1600. [CrossRef]
28. Özacar, M.; Poyraz, A.S.; Genuino, H.C.; Kuo, C.-H.; Meng, Y.; Suib, S.L. Influence of Silver on the Catalytic Properties of the Cryptomelane and Ag-Hollandite Types Manganese Oxides OMS-2 in the Low-Temperature CO Oxidation. *Appl. Catal. A Gen.* **2013**, *462–463*, 64–74. [CrossRef]
29. Li, X.; Ma, J.; Zhang, C.; Zhang, R.; He, H. Facile Synthesis of Ag-Modified Manganese Oxide for Effective Catalytic Ozone Decomposition. *J. Environ. Sci.* **2019**, *80*, 159–168. [CrossRef]
30. Wang, Z.; Jia, H.; Cai, H.; Qi, J. Highly Conductive Mn_3O_4/MnS Heterostructures Building Multi-Shelled Hollow Microspheres for High-Performance Supercapacitors. *Chem. Eng. J.* **2020**, *392*, 123890. [CrossRef]
31. Xiong, P.; Zhang, F.; Zhang, X.; Wang, S.; Liu, H.; Sun, B.; Zhang, J.; Sun, Y.; Ma, R.; Bando, Y.; et al. Strain Engineering of Two-Dimensional Multilayered Heterostructures for Beyond-Lithium-Based Rechargeable Batteries. *Nat. Commun.* **2020**, *11*, 3297. [CrossRef] [PubMed]
32. Ma, X.; Cheng, J.; Dong, L.; Liu, W.; Mou, J.; Zhao, L.; Wang, J.; Ren, D.; Wu, J.; Xu, C.; et al. Multivalent Ion Storage Towards High-Performance Aqueous Zinc-Ion Hybrid Supercapacitors. *Energy Storage Mater.* **2019**, *20*, 335–342. [CrossRef]
33. Zhou, Y.; Cheng, X.; Huang, F.; Sha, Z.; Han, Z.; Chen, J.; Yang, W.; Yu, Y.; Zhang, J.; Peng, S.; et al. Hierarchically Structured Electrodes for Moldable Supercapacitors by Synergistically Hybridizing Vertical Graphene Nanosheets and MnO_2. *Carbon* **2021**, *172*, 272–282. [CrossRef]
34. Fang, Q.; Sun, M.; Ren, X.; Cao, B.; Shen, W.; Li, Z.; Fu, Y. Ultrafine Mn_3O_4 Nanowires Synthesized by Colloidal Method as Electrode Materials for Supercapacitors with a Wide Voltage Range. *J. Energy Storage* **2021**, *44*, 103260. [CrossRef]
35. Fang, Z.; Xu, M.; Li, Q.; Gu, J.; Wang, J.; Wang, D. Over-Reduction-Controlled Mixed-Valent Manganese Oxide with Tunable Mn^{2+}/Mn^{3+} Ratio for High-Performance Asymmetric Supercapacitor with Enhanced Cycling Stability. *Langmuir* **2021**, *37*, 2816–2825. [CrossRef]
36. Minakshi, M.; Higley, S.; Baur, C.; Mitchell, D.R.G.; Jones, R.T.; Fichtner, M. Calcined Chicken Eggshell Electrode for Battery and Supercapacitor Applications. *RSC Adv.* **2019**, *9*, 26981–26995. [CrossRef]
37. Anjana, P.M.; Kumar, S.R.S.; Rakhi, R.B. Manganese Cobalt Oxide Nanoflakes for Electrochemical Energy Storage. *J. Mater. Sci. Mater. Electron.* **2022**, *33*, 8484–8492. [CrossRef]
38. Shi, S.; Wan, G.; Wu, L.; He, Z.; Wang, K.; Tang, Y.; Xu, X.; Wang, G. Ultrathin Manganese Oxide Nanosheets Uniformly Coating on Carbon Nanocoils as High-Performance Asymmetric Supercapacitor Electrodes. *J. Colloid Interface Sci.* **2019**, *537*, 142–150. [CrossRef]
39. Hsieh, C.E.; Chang, C.; Gupta, S.; Tai, N.H. Binder-Free $CoMn_2O_4$/Carbon Nanotubes Composite Electrodes for High-Performance Asymmetric Supercapacitor. *J. Alloys Compd.* **2022**, *897*, 163231. [CrossRef]
40. Yan, L.; Niu, L.; Shen, C.; Zhang, Z.; Xu, S. Modulating the Electronic Structure and Pseudocapacitance of δ-MnO_2 through Transitional Metal M (M=Fe, Co and Ni) Doping. *Electrochim. Acta* **2019**, *306*, 529–540. [CrossRef]